OXFORD

ARTICLE

Whole-Body and Microenvironmental Localization of Radium-223 in Naïve and Mouse Models of Prostate Cancer Metastasis

Diane S. Abou, David Ulmert, Michele Doucet, Robert F. Hobbs, Ryan C. Riddle, Daniel L. J. Thorek

Affiliations of authors: Division of Nuclear Medicine and Molecular Imaging, Department of Radiology and Radiological Science (DSA, DLJT), Department of Orthopaedic Surgery (MD, RCR), Department of Radiation Oncology (RFH), and Cancer Molecular and Functional Imaging Program, Department of Oncology (RFH, DLJT), Sidney Kimmel Comprehensive Cancer Center, The Johns Hopkins University (JHU) School of Medicine, Baltimore, MD; Program in Molecular Pharmacology and Chemistry, Memorial Sloan Kettering Cancer Center, New York, NY (DU); Department of Clinical Sciences (Urology), Lund University, Skåne University Hospital, Malmö, Sweden (DU).

Correspondence to: Daniel L. J. Thorek, PhD, Division of Nuclear Medicine and Molecular Imaging, Department of Radiology and Radiological Science, Johns Hopkins University School of Medicine, 720 Rutland Avenue, Ross Building Room 220, Baltimore, MD, 21205 (e-mail: dthorek1@jhmi.edu).

Abstract

Background: Bone-metastatic, castration-resistant prostate cancer (bmCRPC) represents a lethal stage of the most common noncutaneous cancer in men. The recent introduction of Radium-223 dichloride, a bone-seeking alpha particle (α)–emitting radiopharmaceutical, demonstrates statistically significant survival benefit and palliative effect for bmCRPC patients. Clinical results have established safety and efficacy, yet questions remain regarding pharmacodynamics and dosing for optimized patient benefit.

Methods: We elucidated the biodistribution of ^{223}Ra as well as interaction with the bone and tumor compartments in skeletally mature mice (C57Bl/6 and CD-1, n = 3–6) and metastasis models (LNCaP and PC3, n = 4). Differences in uptake were evaluated by µCT and histological investigation. Novel techniques were leveraged on whole-mount undecalcified cryosections to determine microdistribution of Radium-223. All statistical tests were two-sided.

Results: ^{223}Ra uptake in the bones (>30% injected activity per gram) at 24 hours was also accompanied by non-negligible remnant activity in the kidney (2.33% ± 0.36%), intestines (5.73% ± 2.04%), and spleen (10.5% ± 5.9%) Skeletal accumulation across strains did not correspond with bone volume or surface area but instead to local blood vessel density (P = .04). Microdistribution analysis by autoradiography and α camera revealed targeting of the ossifying surfaces adjacent to the epiphyseal growth plate. In models of PCa metastasis, radioactivity does not localize directly within tumors but instead at the apposite bone surface. Osteoblastic and lytic lesions display similar intensity, which is comparable with uptake at sites of normal bone remodeling.

Conclusions: Profiling the macro- and microdistribution of ^{223}Ra in healthy and diseased models has important implications to guide precision application of this emerging α-therapy approach for bmCRPC and other bone metastastic diseases.

Prostate cancer (PCa) is the most commonly diagnosed cancer among men, with over a quarter of a million new cases in 2014 in the United States alone (1). Initially sensitive to endocrine therapy, the disease invariably overcomes these approaches and the fatal stage of the disease is characterized by strong tropism to the skeleton (2). PCa mortality is strongly influenced by bone metastasis and its associated skeletal-related events (SRE), decreased bone strength, malignant compression fracture, debilitating pain, and marrow failure as metastases displace the haematological compartment (3).

Treatment of bone-metastatic, castrate-resistant prostate cancer (bmCRPC) may involve bisphosphonates, androgen receptor antagonists, biological, and radiopharmaceuticals. Bisphosphonates and the anti-RANKL antibody denosumab act on the bone microenvironment and reduce incidence of SRE. However, they neither prevent metastasis nor improve progression-free or overall survival (4,5). Beta particle (β)–emitting Strontium-89 and Samarium-153 Lexidronam both target areas of bone turnover and are approved for bone pain palliation but likewise fail to extend survival (6).

Recently, Radium-223 dichloride (^{223}RaCl$_2$) demonstrated median survival extension in bmCRPC of 3.5 months vs placebo (7) and gained approval for patients free of visceral disease (8). Through decay of the 11.4 day half-life ^{223}Ra and its daughters a total of four alpha particles (α) are emitted, which are helium nuclei with high linear energy transfer (LET) properties (Figure 1). The weighted average energy of αs from the ^{223}Ra decay chain is 5.78 MeV, and this dose is deposited with an average travel of merely 57 μm (9,10). The result is exquisitely cytotoxic radiation highly localized to the distribution of the radionuclide.

Radium is described as a calcium mimetic with bone-seeking properties (11). It localizes to bone matrix but avoids myeloablative effects because the short α range largely spares the marrow compartment (12), unlike aforementioned β emitters. However, the strong proximity dependence of αs raises questions regarding the mechanism(s) of action leading to survival gains and palliative response (7). Understanding the properties of ^{223}RaCl$_2$ and its radiobiological effects is needed to achieve the maximum effective use of this new therapy, especially as investigations of increased activity, dose frequency, and combination treatment approaches are underway (ClinicalTrials.gov: NCT02043678, NCT01934790, NCT02023697).

We hypothesized that healthy and diseased murine models could provide insight to answer outstanding questions regarding parameters that influence ^{223}RaCl$_2$ uptake and function. This has important implications for the design and interpretation of preclinical studies evaluating treatment with ^{223}RaCl$_2$, to guide clinical application with altered dosing and combination treatment, and ultimately for more effective application in men. In this study, we investigated the whole-body distribution of Radium-223 in naïve mice. Using radiological and analytical nuclear techniques, we evaluated the role of bone morphological and vascular characteristics on skeletal uptake. Fresh frozen, undecalcified tissue sections were subjected to conventional autoradiography and α camera imaging to localize ^{223}Ra at sub-organ resolution. Furthermore, these techniques were used to determined uptake at osteoblastic and lytic lesions in prostate cancer bone metastasis models.

Methods

Calibration

^{223}RaCl$_2$ (Bayer HealthCare Pharmaceuticals, Leverkusen, Germany) was calibrated according to guidelines provided by the supplier in response to the Nuclear Regulator Commission (14). Briefly, the dial setting of the calibrator (CRC-127R, Capintec; Ramsey, New Jersey) was determined by selecting a value that was confirmed with the decay-corrected National Institute of Standards and Technology standard calibrated dose upon vialing. This empirically determined dial setting (#277) was used for all experiments. Animals received 150 μL of clinical-grade ^{223}RaCl$_2$ citrate solution, diluted in sterile physiological saline, immediately before injection.
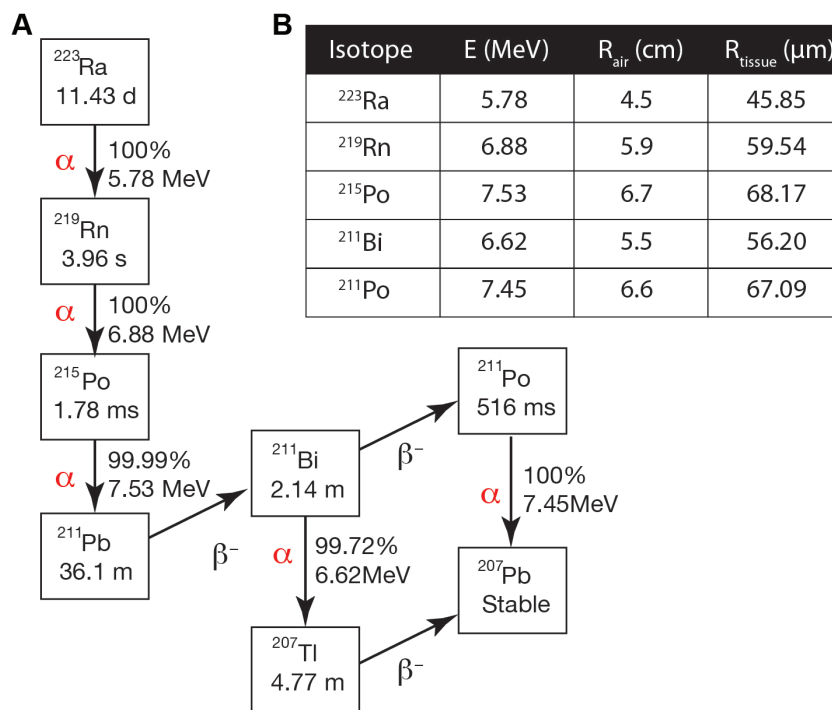
Figure 1. Decay chain and properties of Radium-223. **A)** The predominant alpha (α) and beta (β⁻) particle emissions of Radium-223 and its daughters results in production of four high-energy α emissions per disintigration. For each disintegration, abundance and energy released are presented. The rapid decay of the daughters ensures that dose is deposited at or near the longer-lived, bone-seeking Radium-223 parent. **B)** Alpha particle ranges in air were determined using energies and decay ratios as provided in (30) and computed as per (9). Tissue travel range values were computed using the Bragg-Kleeman rule (10).

Isotope	E (MeV)	R_{air} (cm)	R_{tissue} (μm)
^{223}Ra	5.78	4.5	45.85
^{219}Rn	6.88	5.9	59.54
^{215}Po	7.53	6.7	68.17
^{211}Bi	6.62	5.5	56.20
^{211}Po	7.45	6.6	67.09

Mouse Experimentation

All mice were skeletally mature males (greater than 14 weeks of age). CD-1 mice (Charles River Laboratories), B6.Cg C57Bl/6 mice (Jackson Laboratories; Bar Harbor, ME), and Nu/Nu mice (Harlan Laboratories; Indianapolis, IN) were placed on standard feed ad libitum. All mouse experimentation was in accordance with institutional animal welfare protocols at The Johns Hopkins University School of Medicine. PC3 and LNCaP-AR cells (15) were inoculated intratibially in Nu/Nu mice, as described (16). Bone metastasis was monitored by bioluminescence and x-ray computed tomography (CT) using the IVIS SpectrumCT (Perkin Elmer; Waltham, MA).

Mice were dosed with ^{223}RaCl$_2$ (10 kBq, n = 4–6 per experimentation group) and killed at one, four, or 24 hours for prompt dissection. To determine remnant whole-body activity at these time points, anesthetized mice were placed in a dose calibrator (n = 5). Tissue activity was assayed by gamma (γ) counting or was cryo-embedded (OCT, Sakura Fintec, Torrance, CA). For whole-body autoradiography samples, mice were killed at 24 hours (n = 3). No fixation or decalcification chemicals were applied to mouse tissues, which were either stored (-80˚ C) or flash-frozen in liquid nitrogen. γ-counting energy was set between 240 and 300 keV. The main photopeak detected at 270 keV was provided by ^{223}Ra (269 keV; 13.6%) and ^{219}Rn (271 keV; 9.9%) emissions (Wizard^2, Perkin Elmer). High-resolution μCT (HRμCT), histological and autoradiographic methods are described in the Supplementary Materials (available online).

Statistical Analysis

Statistical evaluation was performed in Prism 5.0D (GraphPad Software; La Jolla, CA) and Excel (Microsoft; Redmond, WA) using an unpaired, two-tailed Student's t test. Differences at the 95% confidence level ($P < .05$) were considered to be statistically significant. Results are presented as mean ± standard deviation, unless stated otherwise.

Results

Organ Distribution of Radium-223 Dichloride

Previous studies in rodents have found minimal (17) or undetectable (18) uptake of ^{223}Ra outside of the calcified tissues. This contrasts with the human planar imaging of therapeutic doses of the radiopharmaceutical, which demonstrated intense abdominal uptake (13). To test the utility of mice as models, we examined the kinetic biodistribution of ^{223}RaCl$_2$ in skeletally mature C57Bl/6 mice. Localization to the bone was rapid, with 1.85% ± 0.49%, 2.86% ± 0.49%, and 4.54% ± 0.65% injected activity (IA) in the tibia, femur, and vertebrae samples after one hour determined by γ-counting (Figure 2A). Bone labeling at four and 24 hours was non-statistically significant from the initial reading, and this confirms previous reports that Radium-223 (and its short-lived daughters) do not redistribute in rodent or man (13,17). We therefore focused our interest on the acute distribution of the radionuclide. Adjusting for the mass of resected tissues for the readings, at 24 hours postadministration we measured 51.19% ± 11.53%, 46.68% ± 5.12%, and 30.78% ± 3.99% IA per gram (%IA/g) in the tibia, femur, and vertebrae, respectively (Figure 2B).

Uptake in the spleen, stomach, and intestinal organs and the expected renal clearance and early bladder passage (genitourinary package) were observed (Figure 2). These results underline the non-negligible levels of ^{223}Ra outside of the bone and reveal that a statistically significant fraction (>25% IA) of the agent rapidly transits to the small and large intestine to be excreted (Figure 2A). ^{223}Ra uptake in the bones (>30% injected activity per gram) at 24 hours was also accompanied by non-negligible remnant activity in the kidney (2.33% ± 0.36%), intestines (5.73% ± 2.04%), and spleen (10.5% ± 5.9%) (Figure 2B).

Whole-body clearance was monitored using a well counter (Figure 2C). Combined renal and intestinal clearance resulted in retention of 81% ± 5% of the IA at one hour, which decreased at four hours to 76% ± 3% and fell further at 24 hours to only 46.5% ± 2%. These values resemble those determined in a phase I pharmacokinetic study in men with bmCRPC (13) and validate the use of skeletally mature rodents as a model to study Radium-223 in men.

To verify γ counts, whole-body autoradiography visually confirmed soft-tissue and skeletal uptake. Standard tissue processing for histochemistry and evaluation (including fixation and decalcification) would remove ^{223}Ra or alter the radionuclide distribution. Thus, mice were killed and flash frozen at 24 hours postinjection, prior to unfixed and undecalcifed sectioning. Macrographs, autoradiography, and overlay are shown for representative sections (Figure 2, D-F). Direct imaging corroborates γ counts with prominent ^{223}Ra labeling of the skeleton, spleen, stomach, and kidneys.

Radium-223 Uptake and Bone Microstructure

Autoradiography and γ counting revealed non-negligible soft-tissue uptake (Figure 2). C57Bl/6 mice are known to be osteopenic relative to other strains (19), and it is conceivable that use of this low-bone model may bias ^{223}Ra results towards lower bone uptake and greater intestinal accumulation. To interrogate the role of bone phenotype on uptake, we evaluated distribution in a second common strain. Skeletally mature, age-matched, male C57Bl/6 and CD-1 mice were dosed with ^{223}RaCl$_2$, and distribution was evaluated.

Uptake was not statistically significant between the strains for any of the soft tissues (Figure 3, A and B). The minimum statistical test value across the soft tissues was the small intestine (%IA/g, $P = .39$). However, greater labeling in the C57Bl/6 strain was noted in the skeleton, in total counts, when compared with CD-1 uptake (Figure 3A). These differences were statistically significant for the femur ($P < .001$) and tibia ($P = .04$) and trended in that direction for the vertebrae. The distinction between the two strains was magnified when adjusting for bone mass (%IA/g) (Figure 3B) as C57Bl/6 have reduced skeletal volume. Indeed, C57Bl/6 mice (14.72 ± 0.11 mm) have grossly smaller femur length than that of the CD-1 strain (15.62 ± 0.26 mm, $P = .04$) (Figure 3B insert).

This greater uptake in smaller bone tissue was unexpected. We suspected that mouse strain–dependent features of bone microarchitecture might explain the difference in ^{223}Ra distribution. To ask this question, we undertook detailed HRμCT of the trabecular and cortical regions of the femur and tibia (femur schematic) (Figure 3C). The bone volume of the CD-1 was greater than that of the C57Bl/6 in the trabecular and cortical regions of the femur (Figure 3, D and F). Quantitative analysis confirmed that the CD-1 strain exhibits greater total tissue volume (5.31 ± 0.95 mm^3 vs 3.56 ± 0.20 mm^3; $P = .02$) and occupying bone volume (1.081 ± 0.18 mm^3 vs 0.781 ± 0.11 mm^3; $P = .04$) in the cancellous bone than C57Bl/6. However, there was no difference in the density or thickness of trabecular structures ($P = .21$). Consequently, bone as a percent of the total tissue volume (BV/TV)
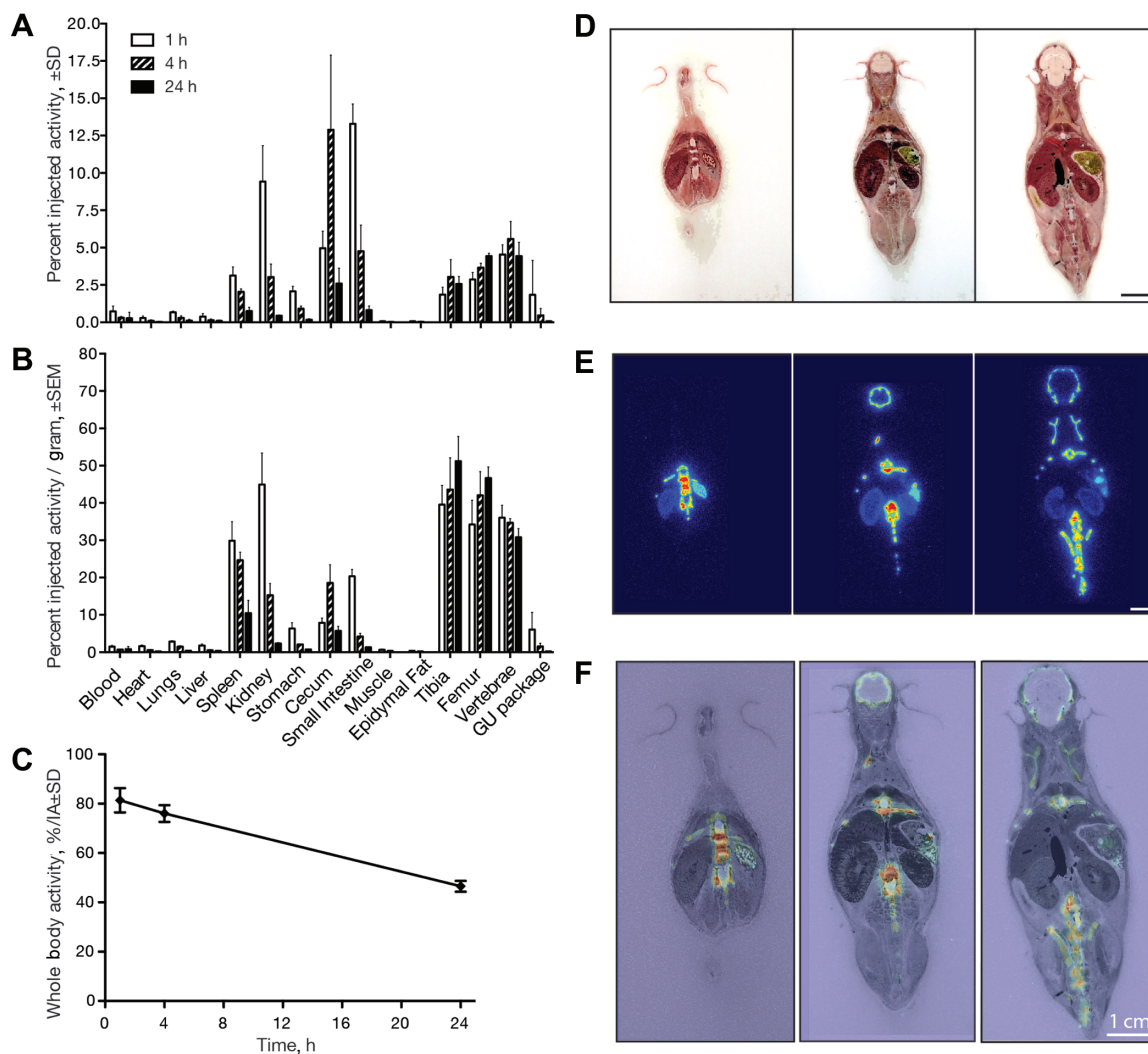
Figure 2. Dynamic organ-level distribution of Radium-223 evaluated in skeletally mature male CD-1 mice. Mice (n = 4–5 per group) were killed at one, four, and 24 hours postinjection, and organs evaluated for activity by γ counting. **A)** The distribution is expressed in percent injected activity (%IA ± SD) representing the amount in each organ relative to the administered dose and **(B)** normalized to the weight of each organ (%IA/g ± standard error of the mean). **C)** ^{223}Ra clearance profile was defined measuring whole-body radioactive content over 24 hours. **D-F)** To confirm ex vivo γ count results, whole-body undecalcified cryosections (14 µm) were obtained at 24 hours after administration. Autoradiography revealed skeletal uptake in the calvaria and vertebrae, while soft tissue accumulation is recapitulated in the spleen and kidney. **Scale bars** = 1 cm.

was not statistically significantly different, at approximately 20% (*P* = .35) (Figure 3E). Similar results were determined from quantitative analysis in the cortical region. The amount of total tissue in the CD-1 was statistically significantly greater than the C57Bl/6 (2.33 ± 0.137 mm^2 compared with 1.73 ± 0.077 mm^2; *P* = .02) while the cortical area fraction, or bone-to-tissue area ratio, does not vary statistically significantly, at nearly 45% (*P* = .09) (Figure 3G). Therefore, the paradoxically greater uptake in smaller bones could not be explained by a bone tissue area balance at the micron scale; CD-1 mice have statistically significantly more total bone and bone surface area yet lower ^{223}Ra uptake.

Vascular Dependence of Uptake

^{223}RaCl$_2$ was rapidly cleared from the blood (Figure 2, A and B), and we next tested the hypothesis that discrepant skeletal uptake could be attributed to differences in vascular delivery. We determined the vascular density by CD-31 staining (Figure 4A).

The number of vessels in the trabecular compartment was computed by counting the number of CD31-positive vessels in 40 high-powered fields in the tibia and femur. The C57Bl/6 samples had a greater vascular density of CD31-positive vessels than that of CD-1 (Figure 4B). There was an approximately 28% ± 8% increase in the number of blood vessels per mm^2 across age- and sex-matched mice from the two strains (*P* = .04). No statistically significant difference was found in the marrow cavity (data not shown). These results suggest that a dominant characteristic for the magnitude of ^{223}Ra uptake at bone sites is blood vessel density dependent rather than the quantity of exposed bone surface area or bone volume.

Radium-223 Microdistribution

We next explored microscopic Radium-223 distribution. Intact hind limbs of naïve mice were cryosectioned 24 hours following dosing by ^{223}RaCl$_2$ and scanned by α camera. A representative section is shown, including: en bloc macrograph of the
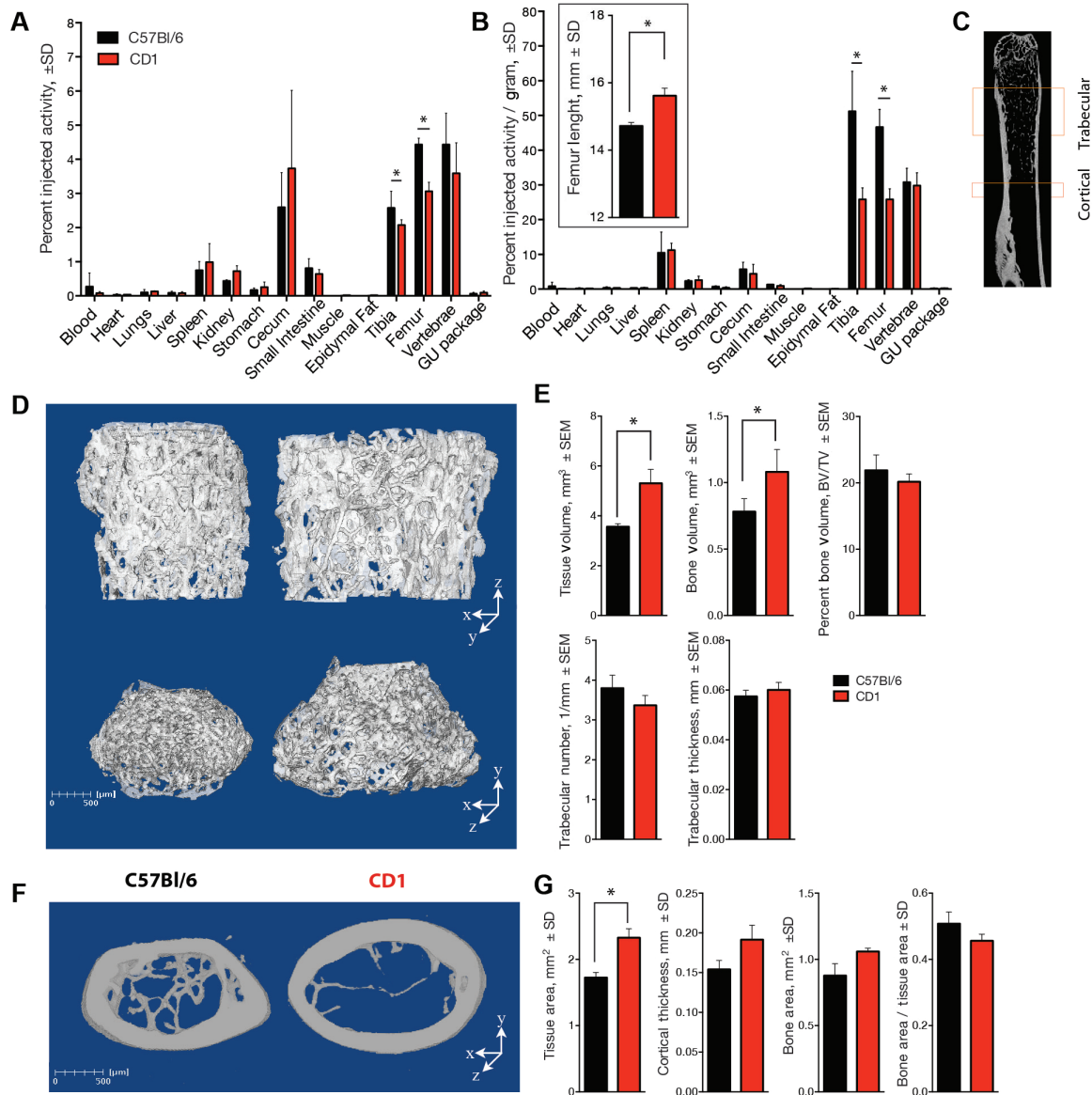
Figure 3. Strain-dependent differences in Radium-223 uptake and bone microarchitecture. **A)** The distribution of the radionuclide was compared in age- and sex-matched C57Bl/6 and CD-1 (n = 5) as percent injected activity %IA ± SD. **B)** The greater overall uptake in the smaller long bones of the C57Bl/6 strain (insert) is enhanced when normalized to tissue mass (%IA/g ± SD). **C)** Regions of cortical and trabecular compartments for analysis by μCT. Three-dimensional bone volume from representative samples of **(D)** the trabecular (at two perspectives) and **(F)** cortical regions of the femur (**scale bars** = 500 μm). **E)** Quantitative μCT analysis of the distal femur reveals the larger tissue and bone volume of the CD-1 mice. The bone density bone volume fraction (BV/TV ± standard error of the mean) and other morphologic parameters of the trabeculae do not meet statistical significance; therefore, there is incontrovertibly greater bone area in the CD-1 mice. **G)** Likewise, analysis of the cortical bone establishes the greater size of the CD-1 (tissue and bone area ± SD) to that of C57Bl/6, despite the two strains having similar cortical area fraction values (bone/tissue area ± SD). Statistical significance was determined using an unpaired two-tailed Student's t test; *P < .05.

sample cutting surface on the cryostat, a white light reflectance image of the tissue section in the α camera, α exposure, and overlay (Figure 5, A-D). The system resolution (~50 μm; measured using a optical line target) revealed localization predominantly to the distal femur and proximal tibia, with little activity in the marrow cavity or cortical bone surface. Safranin-O differentiates mineral bone (in green) from proteoglycans and cartilage (in red-orange). Binding to the cartilage itself is not observed, either at the growth plate or at the articular surfaces of the joints (Figure 5E). ^{223}Ra distribution colocalized with the freshly mineralized osteoid matrix characterized by a very high bone modeling/remodeling activity directly at the front of the growth plate.

Radium-223 and Bone Metastasis Models of Prostate Cancer

Using an intratibial inoculation model of metastasis, we evaluated the acute microdistribution of ^{223}Ra with osteoblastic (LNCaP) and osteolytic (PC3) PCa lines. En bloc macrophotographs and cryosections were exposed and developed histochemically (hematoxylin and eosin, Safranin-O) for tissue morphology identification (Figure 6). Representative autoradiograms demonstrate that ^{223}Ra does not localize directly to the tumor (indicated by arrow), regardless of type. Instead, activity accumulates at the apposite bone surface surrounding the lesion, as well as again at the active bone modeling/remodeling
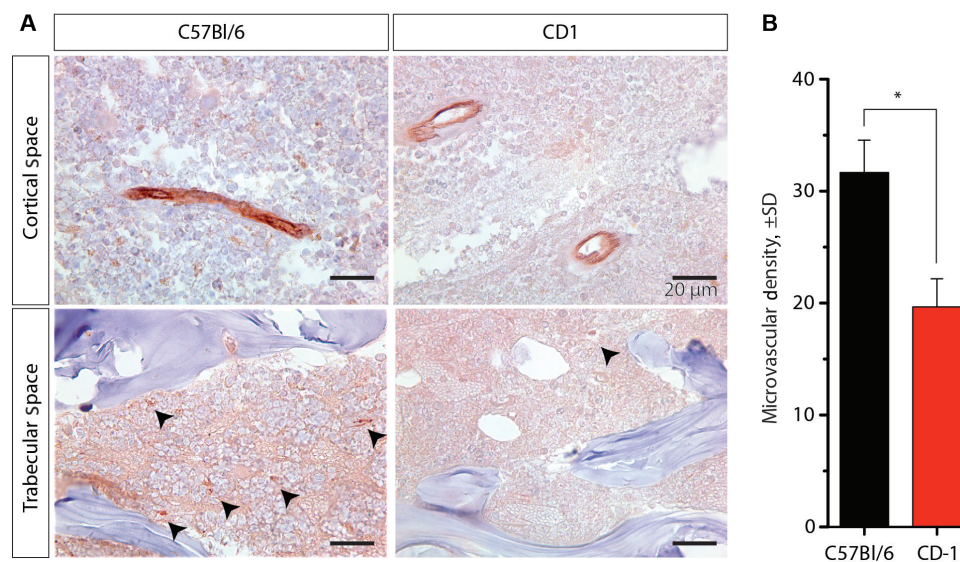
Figure 4. Endothelial cell (CD-31) immunohistochemistry of paraffin-embedded bone sections. **A)** Vessels identified in the C57Bl/6 and CD-1 strains of mice (n = 3 per strain) in the trabecular and cortical compartments, indicated by **arrowhead (scale bar** = 20 μm). **B)** Quantification of microvessel density as number of vessels per mm². **Error bars** represent SD, and statistical significance was determined using an unpaired two-tailed Student's *t* test; *P < .05.

sites. The ^{223}Ra deposition in healthy bone sites is likewise equivalent to the levels in bone surrounding the tumors. Further, alkaline phosphatase enzyme stain (ALP) colocalized osteoblastic activity and ^{223}Ra uptake at both the malignant and joint site (Supplementary Figure 1, available online).

Discussion

Metastatic invasion of the skeleton in PCa results in pain, risk of fracture, and bone marrow failure. ^{223}RaCl$_2$ provides selective and effective treatment of bmCRPC lesions. Currently administered based upon body weight—independent of disease characteristics—there is an urgent need to develop personalized treatment plans. Rodent models have provided considerable value in development of bmCRPC drug candidates (15,20). However, there is scant literature evaluating ^{223}RaCl$_2$ in preclinical models of PCa, with notable exceptions (18). Our investigation focused on understanding the pharmacodynamics of ^{223}Ra and the development of tools to enable its detailed study at multiple scales.

Whole-body ^{223}Ra distribution was determined and compared with bone features including HRμCT and vasculature morphology. The skeletally mature mice (age >14 weeks) used in this work possess normalized bone growth and resorption rates (21). The epiphyseal plates of mice do not fuse, and ^{223}Ra accumulation was noted at sites of bone activity—whether adjacent to the growth plate or surrounding implanted intraosseous xenografts. Along with expected skeletal accumulation, non-negligible uptake in the spleen, intestines, and kidney was quantified and imaged and corresponded with the gastrointestinal accumulation seen in men using planar γ-scintigraphy (13,22). Clinical effects of uptake at these sites are associated with reported adverse gastrointestinal events, often leading to cessation of treatment (23). Acknowledging differences between mouse and human bone properties, these results provide support for the use of skeletally mature mouse models as surrogates to evaluate the impact of Radium-223 (24).

Statistically significantly greater ^{223}Ra %IA (P < .04) and %IA/g (P < .001) in the tibia and femur of smaller C57Bl/6 over CD-1 mice was observed. C57Bl/6 mice possess less bone volume and

area but similar bone density and trabecular number, ruling out a morphometric explanation for the unexpected result. ^{223}Ra has a short circulation time, and enhanced uptake may be the result of the greater C57Bl/6 microvascular density determined by anti-CD31 staining. There was no statistically significant difference in uptake in the vertebrae; however, differences in the appendicular and axial skeleton, as well as the difficulty in fully removing soft-tissue from the spine, may explain this result.

α-therapy's short-range and high LET distinguish it from previous approved endoradiotherapies. The abundance-weighted average distance of α emissions from the ^{223}Ra decay chain is 57 μm (R$_{tissue}$), leading us to focus on microstructural localization of the agent. Previous reports of suborgan distribution are limited to investigation of $^{224/226}$Ra isotopes by solution autoradiography in fixed, methyl-methacrylate-embedded specimens (25,26) or scanning photometry (27), not readily available techniques. Using autoradiography and advancing a recently described α camera system (28), ^{223}Ra distribution was imaged at physiological doses. In the metabolically active sites of the mouse skeleton, such as the distal femur and proximal tibia, ^{223}Ra localized to the ossification sites contiguous to the growth plate (Figure 5).

Imaging ^{223}Ra directly is difficult in patients, and questions remain regarding uptake across patients and between lesions. An intratibial inoculation model was used to evaluate the acute microdistribution in models of PCa bone metastasis with both an osteoblastic (LNCaP) and osteolytic (PC-3) phenotype. At bone adjacent to the intraosseous tumors, bone remodeling was confirmed by safarinin-O and ALP (Supplemental Figure 1, available online) and colocalized with ^{223}Ra-labeling (Figure 6). Uptake in the bone microenvironment surrounding metastases occurred at a similar intensity for both osteoblastic and osteolytic tumors. This may have important implications as α-therapy is applied to other osteotropic malignancies including breast, renal, lung, and thyroid carcinoma.

Localization to malignant sites was similar in intensity to the background activity at the epiphyses. This presents a limitation for use of mice as a surrogate for man in studying the whole-body effects of ^{223}Ra but may enable study of radiobiological effects at sites of non-tumor-involved bone activity
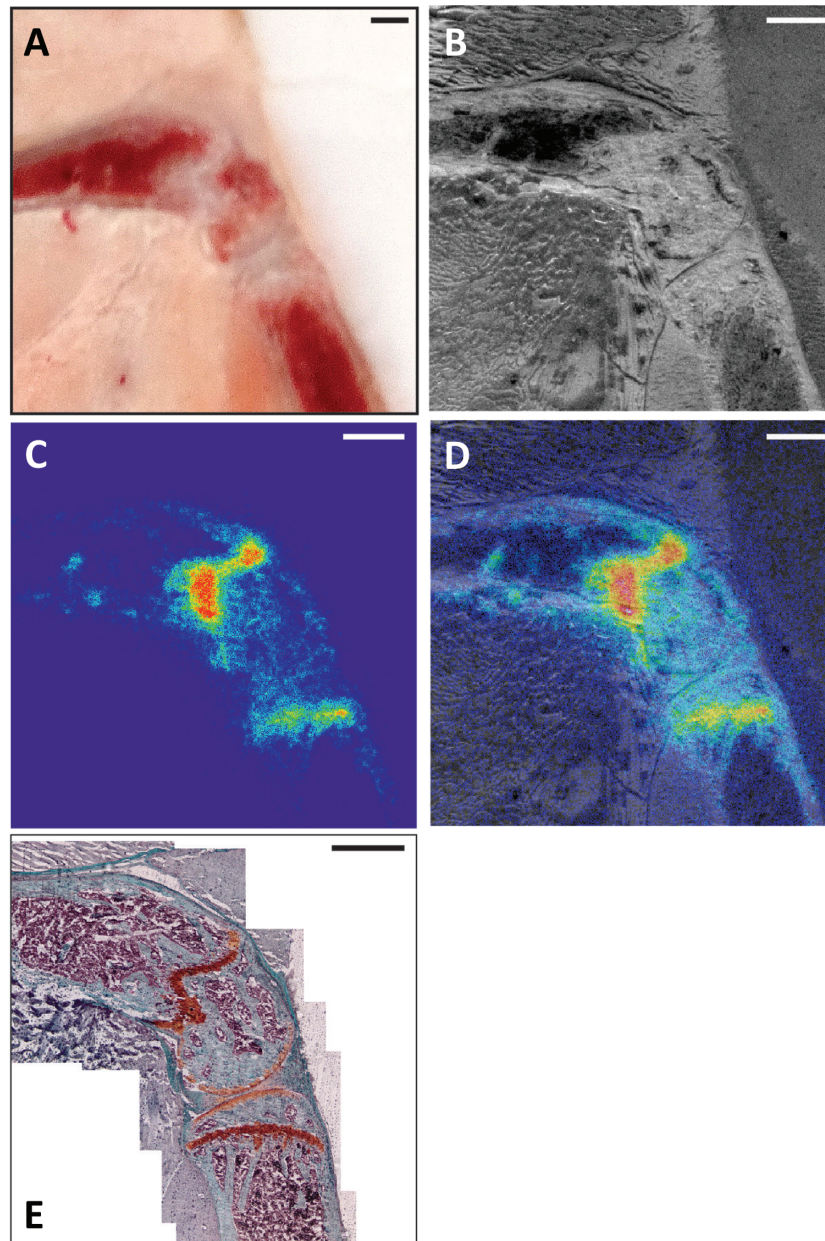
Figure 5. Undecalcified whole-mount cryosection and alpha camera autoradiography of distal femur and proximal tibia. **A)** En bloc color macrophotograph of embedded sample at the cutting surface. **B)** White-light reflectance image of alpha-scintillant mounted section (14 μm) in α camera. **C)** α camera acquisition of Radium-223 (and α-emitting daughters) distribution in sample. **D)** α emission image overlaid with reflectance image. **E)** Composite microscope image of Safranin-O histology revealing mature bone (**green**) and uncalcified proteoglycans (**orange**) at the growth plate, adjacent to the ossification front. Representative result of n = 6; **scale bars** = 500 μm.

(such as at degenerative skeletal foci found throughout the geriatric cancer population). From the preclinical perspective, these results underline that antineoplastic effect may be dependent on tumor model parameters including metastasis volume, distance to vascularized bone surfaces, and tumor placement. Models using lesions directly adjacent to epiphyseal plate will be irradiated by [223]Ra, which may complicate evaluation (29). To match the clinical indication, we examined [223]Ra localization to bone lesions using intraosseous inoculation (exempt of visceral disease that accompanies systemic PCa cell injection). Other bone metastatic models or techniques may be useful to evaluate alternate contexts such as the degree of localization to incipient lesions (prior to fracture) or in the axial skeleton.

There is considerable interest in altered [223]Ra dosing or combination therapies. In this setting, microdistribution analysis coupled to therapeutic outcome may indicate strategies that maximize response. Long-term treatment studies in these mouse models are currently ongoing. Our results here suggest that increases in activity will contribute dose around the metastasis rather that throughout the lesion, that resorptive lesions may be valid targets for [223]Ra, and that compromising vascular access to bone lesions may reduce [223]Ra delivery. Ongoing clinical trials using [223]Ra in combination with antiangiogenic tyrosine kinase inhibitors or Tasquinimod may shed more light on the connection between treatment efficacy and osteovasculature (NCT02406521 and NCT02406521).
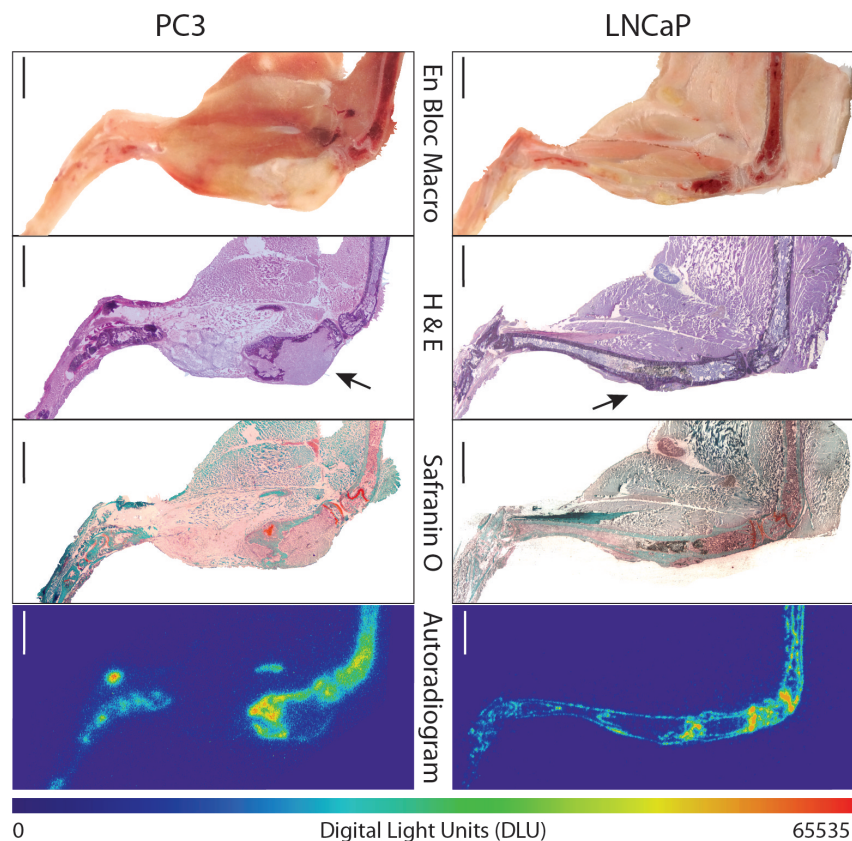
Figure 6. Undecalcified whole-mount cryosection and autoradiography of osteoblastic (LNCaP) and osteolytic (PC3) intratibial prostate cancer xenograft models (n = 3–4 mice per group). En bloc color macrophotograph of embedded sample at the cutting surface. Haematoxylin and eosin (H&E) stain of the whole-mount adhesive bound section, tumor indicated by **arrow**. Safranin-O staining for calcified (**green**) and uncalcified (**orange-brown**) regions. Autoradiography of Radium-223 and daughter emission. Areas of intense uptake colocalize with active bone modeling/remodeling sites (at the interface of the calcified and uncalcified compartments) in the distal femur, proximal tibia, and the bone surfaces adjacent to the bone metastasis. **Scale bars** = 1mm.

We investigated the features of ^{223}Ra distribution in healthy and diseased mice to establish their use towards improved application of this clinical bone-seeking α emitter. Quantitative biodistribution revealed an uptake profile closely matching man at the organ scale. Utilizing microstructural, histological, and emerging nuclear imaging tools, we have established suborgan ^{223}Ra deposition to areas of metabolically active bone with a dependence on local blood vessel density. Our results encourage further use of advanced preclinical models and the techniques developed here to guide combination treatment paradigms and application to other malignancies.

Funding

Notes

The funders had no role in the design of the study; the collection, analysis, or interpretation of the data; the writing of the manuscript; or the decision to submit the manuscript for publication.

The authors declare no conflicts. RFH has previously served as a consultant for Algeta ASA, purchased by Bayer HealthCare Pharmaceuticals, Inc. (Whippany, NJ), which manufactures and distributes Xofigo.

References

1. Siegel R, Ma J, Zou Z, et al. Cancer statistics, 2014. *CA Cancer J Clin.* 2014;64(1): 9–29.
2. Lange PH, Vessella RL. Mechanisms, hypotheses and questions regarding prostate cancer micrometastases to bone. *Cancer Metastasis Rev.* 1998;17(4):331–336.
3. Sathiakumar N, Delzell E, Morrisey MA, et al. Mortality following bone metastasis and skeletal-related events among men with prostate cancer: a population-based analysis of US Medicare beneficiaries, 1999–2006. *Prostate Cancer Prostatic Dis.* 2011;14(2):177–183.
4. Saad F, Gleason DM, Murray R, et al. A randomized, placebo-controlled trial of zoledronic acid in patients with hormone-refractory metastatic prostate carcinoma. *J Natl Cancer Inst.* 2002;94(19):1458–1468.
5. Smith MR, Saad F, Coleman R, et al. Denosumab and bone-metastasis-free survival in men with castration-resistant prostate cancer: results of a phase 3, randomised, placebo-controlled trial. *Lancet.* 2012;379(9810):39–46.
6. Roque IFM, Martinez-Zapata MJ, Scott-Brown M, et al. Radioisotopes for metastatic bone pain. *Cochrane Database Syst Rev.* 2011;(7):CD003347.
7. Parker C, Nilsson S, Heinrich D, et al. Alpha emitter radium-223 and survival in metastatic prostate cancer. *N Engl J Med.* 2013;369(3):213–223.

8. Kluetz PG, Pierce W, Maher VE, et al. Radium Ra 223 dichloride injection: U.S. Food and Drug Administration drug approval summary. *Clin Cancer Res*. 2014;20(1):9–14.

9. Cherry SR, Sorenson JA, Phelps ME, et al. *Physics in nuclear medicine. 3rd ed*. Philadelphia, PA: Saunders; 2003.

10. Knoll GF. *Radiation detection and measurement. 2nd ed*. New York: Wiley; 1989.

11. Harrison GE, Howells GR, Pollard J. Comparative uptake and elution of 45Ca, 85Sr, 133Ba and 223Ra in bone powder. *Calcif Tissue Res*. 1967;1(2):105–113.

12. Hobbs RF, Song H, Watchman CJ, et al. A bone marrow toxicity model for (223)Ra alpha-emitter radiopharmaceutical therapy. *Phys Med Biol*. 2012;57(10):3207–3222.

13. Carrasquillo JA, O'Donoghue JA, Pandit-Taskar N, et al. Phase I pharmacokinetic and biodistribution study with escalating doses of (223)Ra-dichloride in men with castration-resistant metastatic prostate cancer. *Eur J Nucl Med Mol Imaging*. 2013;40(9):1384–1393.

14. Commission USNR. Notice of licensing decision on Radium-223 Dichloride (FSME-13-002). In; 2013.

15. Tran C, Ouk S, Clegg NJ, et al. Development of a second-generation antiandrogen for treatment of advanced prostate cancer. *Science*. 2009;324(5928):787–790.

16. Ulmert D, Evans MJ, Holland JP, et al. Imaging androgen receptor signaling with a radiotracer targeting free prostate-specific antigen. *Cancer Discov*. 2012;2(4):320–327.

17. Henriksen G, Fisher DR, Roeske JC, et al. Targeting of osseous sites with alpha-emitting 223Ra: comparison with the beta-emitter 89Sr in mice. *J Nucl Med*. 2003;44(2):252–259.

18. Henriksen G, Breistol K, Bruland OS, et al. Significant antitumor effect from bone-seeking, alpha-particle-emitting (223)Ra demonstrated in an experimental skeletal metastases model. *Cancer Res*. 2002;62(11):3120–3125.

19. Sophocleous A, Sims AH, Idris AI, et al. Modulation of strain-specific differences in gene expression by cannabinoid type 2 receptor deficiency. *Calcif Tissue Int*. 2014;94(4):423–432.

20. Mitrofanova A, Aytes A, Zou M, et al. Predicting Drug Response in Human Prostate Cancer from Preclinical Analysis of In Vivo Mouse Models. *Cell Rep*. 2015;12(12):2060–2071.

21. Ferguson VL, Ayers RA, Bateman TA, et al. Bone development and age-related bone loss in male C57BL/6J mice. *Bone*. 2003;33(3):387–398.

22. Chittenden SJ, Hindorf C, Parker CC, et al. A Phase 1, Open-Label Study of the Biodistribution, Pharmacokinetics, and Dosimetry of 223Ra-Dichloride in Patients with Hormone-Refractory Prostate Cancer and Skeletal Metastases. *J Nucl Med*. 2015;56(9):1304–1309.

23. Jadvar H, Challa S, Quinn DI, et al. One-Year Postapproval Clinical Experience with Radium-223 Dichloride in Patients with Metastatic Castrate-Resistant Prostate Cancer. *Cancer Biother Radiopharm*. 2015;30(5):195–199.

24. Jilka RL. The relevance of mouse models for investigating age-related bone loss in humans. *J Gerontol A Biol Sci Med Sci*. 2013;68(10):1209–1217.

25. Marquart KH. Early ultrastructural changes in osteocytes from the proximal tibial metaphysis of mice after the incorporation of 224 Ra1,2. *Radiat Res*. 1977;69(1):40–53.

26. Marshall JH, Groer PG, Schlenker RA. Dose to endosteal cells and relative distribution factors for radium-224 and plutonium-239 compared to radium-226. *Health Phys*. 1978;35(1):91–101.

27. Polig E, Jee WS, Dell RB, et al. Microdistribution and local dosimetry of 226Ra in trabecular bone of the beagle. *Radiat Res*. 1988;116(2):263–282.

28. Back T, Jacobsson L. The alpha-camera: a quantitative digital autoradiography technique using a charge-coupled device for ex vivo high-resolution bioimaging of alpha-particles. *J Nucl Med*. 2010;51(10):1616–1623.

29. Suominen MI, Rissanen JP, Kakonen R, et al. Survival benefit with radium-223 dichloride in a mouse model of breast cancer bone metastasis. *J Natl Cancer Inst*. 2013;105(12):908–916.

30. Baum EM, Travis SD. *Nuclides and isotopes: chart of the nuclides. 17th ed*. Schenectady, NY: Bechtel: Knolls Atomic Power Laboratory; 2010.

ARTICLE